CrossMark

On the role of wind and tide in generating variability of Pearl River plume during summer in a coupled wide estuary and shelf system

Tingting Zu [a], Dongxiao Wang [a,*], Jianping Gan [b], Weibing Guan [c]

[a] State Key Laboratory of Tropical Oceanography, South China Sea Institute of Oceanology, Chinese Academy of Sciences, Guangzhou 510301, China
[b] Division of Environment & Department of Mathematics, Hong Kong University of Science and Technology, Kowloon, Hong Kong, China
[c] State Key Laboratory of Satellite Ocean Environment Dynamics, Second Institute of Oceanography, State Oceanic Administration, Hangzhou 310012, China

ABSTRACT

A numerical simulation of the buoyant river plume over the Pearl River Estuary (PRE) and adjacent shelf during a typical upwelling favorable wind period of the summer monsoon is utilized to explore the responses of the plume to wind and tide forcing. The model is forced with time-dependent river discharge, wind and tide, and it shows reasonable ability to capture the basic structure and responses of the plume. Additional numerical experiments that are forced without either wind or tide are used to evaluate the relative importance of wind and tide in generating plume variability. Results show that the vertical structure of the plume and the strength of the stratification in the estuary are determined by the combination of the buoyancy forcing associated with river discharge and tidal forcing, and vary with the advection process, while the horizontal shape and spreading of the plume over the shelf are highly influenced by the wind-driven coastal current, and are more susceptible to the change of vertical mixing. Mechanical energy analysis in each dynamical region (upper, middle, lower estuary, and shelf) reveals that this is because the system mainly gains energy from tide (wind) in the estuary (shelf), and loses energy to the bottom friction (internal-shear mixing) in the estuary (shelf). The largest forcing and dissipation terms in the middle PRE, and at the entrances of smaller estuaries such as Huang Mao Hai, are due to tidal forcing, which enables the middle PRE to serve dynamically as the entrance of an estuary, where the transition of the river plume into coastal buoyancy current usually takes place. In addition, the mixing efficiency increases from upper PRE to the shelf and from strong to weak mixing period, thus the plume in the well-mixed upper estuary is not as sensitive to the changes of wind and tide as that over the highly stratified shelf.

© 2014 Elsevier B.V. All rights reserved.

1. Introduction

The formation and evolution of a river plume over the continental shelf in an idealized numerical model without additional external forcing, such as wind, tide, or ambient flow, is characterized as surface-advected plume, with always a bulge of anticyclonic surface current formed near the estuary mouth (Chao and Boicourt, 1986; Fennel and Mutzke, 1997; Yankovsky and Chapman, 1997). In the Northern Hemisphere, after exiting from the estuary, the buoyant plume turns right into a coastal current with a width narrower than the bulge, and flows downstream in the direction of Kelvin wave propagation. This is also defined as a supercritical plume by Chao (1988a) and Kourafalou et al. (1996a), but not often observed in nature (Garvine, 2001). The more commonly observed plume has a slight or no bulge formed at the estuary mouth and the plume-induced coastal current has a similar width as the bulge, and it is defined as a subcritical plume (Chao, 1988a; Kourafalou et al., 1996a). This kind of plume and coastal current could be reproduced by an idealized simulation by adding downstream

(in Kelvin wave sense) ambient coastal current or downwelling favorable wind, or when more realistic geometry is considered (Garvine, 2001).

River plume shows more complex and diverse structures under the influence of wind and tide forcing. During a period of upwelling favorable wind, the plume is advected offshore through Ekman dynamics and upstream (in Kelvin wave sense) by a wind-driven alongshore coastal current (Chao, 1988b; Choi and Wilkin, 2007; Fong and Geyer, 2001; Gan et al., 2009; Garcia-Berdeal et al., 2002; Kourafalou et al., 1996b; Lentz, 2004; Whitney and Garvine, 2005). The shape and spreading of the plume over the shelf vary and respond quickly (within a few hours) to the change of wind direction and strength. Patches of low-salinity water might be formed if reversal of alongshore current appears (Wolanski et al., 1999). Enhanced mixing by wind can influence the vertical and horizontal structures of the plume (Hetland, 2005; Xing and Davies, 1999). On the other hand, the stratification caused by the plume confines the depth of the wind effect in the surface layer and intensifies the Ekman drift within the plume (Gan et al., 2009). Tide also plays a significant role in changing the structure and spreading of the plume by straining and stirring effects and by tidally-modified residual currents (Chao, 1990; Guo and Valle-Levinson, 2007; Simpson,

1997; Simpson et al., 1990; Zu and Gan, 2009). The plume advances and retreats with the tidal current during a tidal cycle. The greatly enhanced mixing by tide retards the horizontal spreading process, and increases the thickness of the plume, while plume induced stratification modified the tidal current in turn.

The structure and spreading of the plume is closely related to vertical mixing, which is greatly influenced by the variation of wind and tide forcing. Chao (1988b) pointed out two types of wind-induced vertical mixing on the plume: one is the enhanced vertical current shear by seaward or upwelling favorable wind, and the other is the advection of heavier (saltier) water atop lighter (fresher) water by landward or downwelling favorable wind. Hetland (2005) revealed the relationship of the structure of a river plume with vertical mixing by an idealized wind-forced river plume system, and evaluated the effects of wind-induced mixing on the plume at different salinity ranges. His results showed that wind mixing had the greatest effect on plume structure at the salinity range of 24–29 psu. MacCready et al. (2009) extended the study by quantitatively evaluating the wind- and tide-induced mixing effects on the Columbia River plume. They compared the relative importance of wind and tide in an estuary and plume region through a mechanical energy budget, and showed that the divergence of tidal pressure work is dominant in the estuary, while in the far field plume region, whether tide or wind works as the dominant forcing term depends on its strength during different periods. Their results demonstrated the need to include both forcing terms in the simulation of river plume in an estuary and shelf coupled system.

The buoyant plume around the Pearl River Estuary (PRE) has a similar situation as that around the Columbia River estuary in that both estuaries are located along shelves which are influenced by the downwelling favorable wind in winter and upwelling favorable wind in summer. The differences are that the large, bell-shaped PRE is about 50-km wide at the entrance and 60-km long in the axial direction (Fig. 1), the Pearl River has a large fresh water discharge through eight distributaries (four northeastern outlets discharge about half of the total river discharge directly into the PRE, and four southwestern ones

discharge directly into the shelf region (Harrison et al., 2008)), and its lower part could be strongly affected by the coastal circulation (Zu and Gan, 2014). Then questions may arise: when the estuary is large (wider than the internal Rossby deformation radius, $R' = \frac{\sqrt{g'h}}{f}$), what is its function in maintaining the mixing rate in transferring fresh water into shelf water? What are the relative roles of wind- and tide-induced mixing in different parts of a large estuary? And how do the plume and related mixing efficiency inside the estuary and over the shelf respond to the change of physical forcing in such a wide estuary and shelf upwelling system? In this paper, we try to answer these questions by expanding the MacCready et al. (2009) study to the PRE region.

The circulation around the PRE and its responses to tide, wind and buoyancy discharge during the dry (winter) and wet (summer) seasons have been investigated numerically (Ji et al., 2011a,b; Wong et al., 2003a,b; Xue and Chai, 2001). However, there are only a few studies focusing on the responses of the river plume to the physical forcing in the PRE, compared to those carried out in other estuaries in the world. The plume shows a distinct seasonal variation (Dong et al., 2004), as it is influenced by a large river discharge (about 10,000–40,000 m^3 s^{-1}) under upwelling favorable wind in summer and by a small discharge (about 1000–5000 m^3 s^{-1}) under strong downwelling favorable wind in winter (Harrison et al., 2008). Hence, its pattern is much more diverse in the wet (summer) season than in the dry (winter) season. The Pearl River plume was characterized into four types, namely, offshore bulge spreading, west alongshore spreading, east offshore spreading, and western and eastern alongshore spreading, by Ou et al. (2007), according to the surface salinity distribution observed between 1978 and 1984. The offshore bulge spreading type seldom appears, and the other three types are observed often and are subcritical plumes. Further study by Ou et al. (2009) showed that the size of the plume was related with the river discharge, and wind played a significant role in changing the shape of the plume. Owing to the temporal and spatial limitation of the observation data, structures and responses of the plume could neither be captured well nor investigated without the aid of a numerical
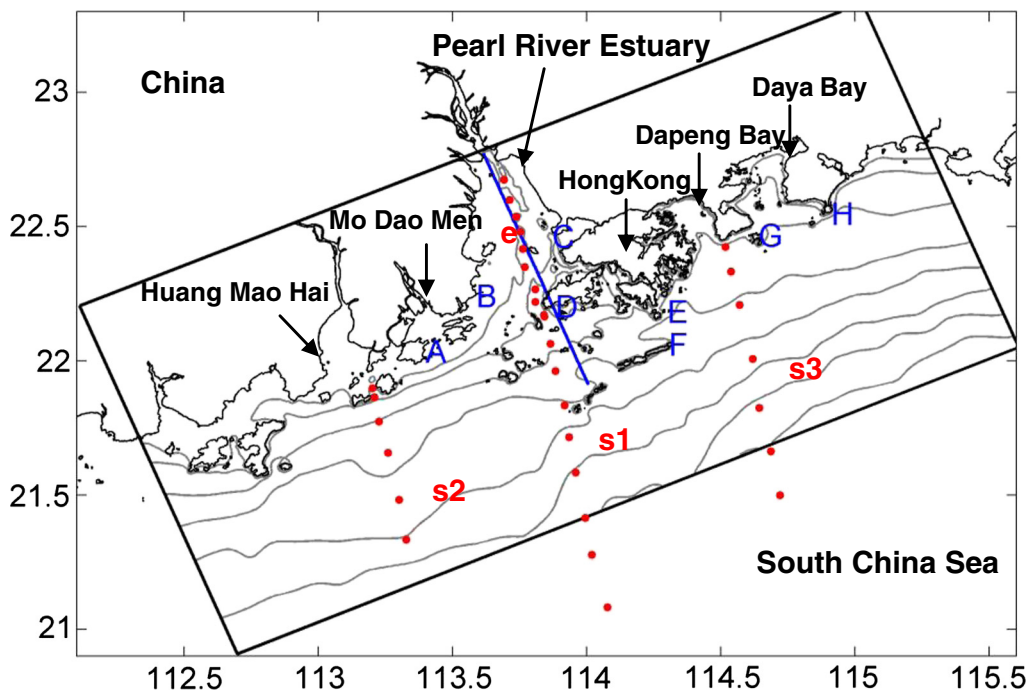

Fig. 1. Model domain (indicated by the rectangular box) and topography (contours for 5, 10, 20, 30, 40, 50, 60 and 70 m isobaths) for the Pearl River Estuary. The blue line marks the axial section of the PRE. Letters A–H indicate the tidal gauge stations used for model validation, and the red dots show the cruise sections s1, s2, s3, and e. (For interpretation of the references to color in this figure legend, the reader is referred to the web version of this article.)

model. Gan et al. (2009) revealed the interactive dynamic processes between the Pearl River plume and upwelling circulation over the Northern SCS shelf using a shelf circulation model. They found that the buoyant plume was advected and reshaped by the coastal current, while the current was also modified by the stratification and pressure gradient induced by the plume. The interaction between the plume and the coastal current establishes a new dynamic balance that shapes the shelf circulation. Zu and Gan (2009), as well as Luo et al. (2012), examined the wind, tide and Coriolis effects on the Pearl River plume by using idealized and realistic topography, respectively, in their numerical simulations. These studies, however, only qualitatively showed the responses of the plume to the forcing field. The quantitative contributions of wind and tide to vertical mixing and related plume structures in different dynamic regions in the wide PRE that receives a large amount of fresh water input remain largely unclear.

In this paper, we explore the spreading and structure of the Pearl River plume in response to upwelling favorable wind, tide, and buoyancy discharge through a high-resolution circulation model that resolves the estuary and part of the shelf sea. Numerical experiments are carried out with energy analysis to differentiate the roles of these physical forcing fields in different geographical regions. Model implementation and validation are described in Section 2. The responses of the plume structure and estuary stratification to different forcing fields are presented in Section 3. Mechanical energy analysis and salt balance are applied to quantitatively assess the relative contribution of wind and tide to vertical mixing and sub-tidal plume structures in Section 4 and 5, while Section 6 summarizes the study.

2. Numerical model and its validation

2.1. Model configuration

The Regional Ocean Modeling System (ROMS; Haidvogel et al., 2000; Shchepetkin and McWilliams, 2005) is used to set up the estuary-shelf circulation system around the PRE. ROMS has been widely used in simulating estuarine circulation and buoyant plumes in different regions all over the world (Hunter et al., 2010; Li et al., 2005; Liu et al., 2009; MacCready et al., 2009; Otero et al., 2008; Rong and Li, 2012; Warner et al., 2005). The model domain (Fig. 1) covers both the PRE and its adjacent shelf, and the bottom topography is obtained by combining water depth data from the Hong Kong Maritime Department and water depths digitized from the high-resolution navigation charts published by the China Maritime Safety Administration. The average horizontal grid size is about 0.8×0.8 km^2, and a terrain-following s-coordinate (Song and Haidvogel, 1994) with 30 vertical levels and $\theta_S = 2.5$, $\theta_B = 0.8$ are chosen in order to have a higher resolution in both surface and bottom boundary layers. Mellor and Yamada's (1982) level 2.5 turbulent closure scheme is used to parameterize the vertical mixing. Other turbulent closure schemes (e.g., k-kl, k-ε) are also tested, and results show that the structure and spreading of the plume is not sensitive to these turbulent closure schemes compared to the physical forcing (figures not shown). The model starts from 1st June, 2000, and runs for 85 days. Numerous experiments show that it takes about 25 days for the salinity in the PRE to be adjusted to a quasi-steady state, and we use the results after 50 days for further anlaysis in the paper. The model is forced by time-dependent river discharge, wind, and eight major tide components (M$_2$, K$_1$, S$_2$, O$_1$, N$_2$, P$_1$, K$_2$, and Q$_1$), which are extracted from the SCS tidal assimilation model (Zu et al., 2008) (Fig. 2). The wind (obtained in the Waglan Island, shown by Station E in Fig. 1) and initial conditions (obtained by averaging the temperature and salinity profile from World Ocean Atlas 2001 over the shelf region outside the PRE) are applied horizontally uniform over the model domain. The heat and salt fluxes at the sea surface are disregarded in the simulation for simplicity as the aim of this study is to differentiate the roles of wind and tide on the plume. Other details of the model can also be seen in Zu and Gan (2014).
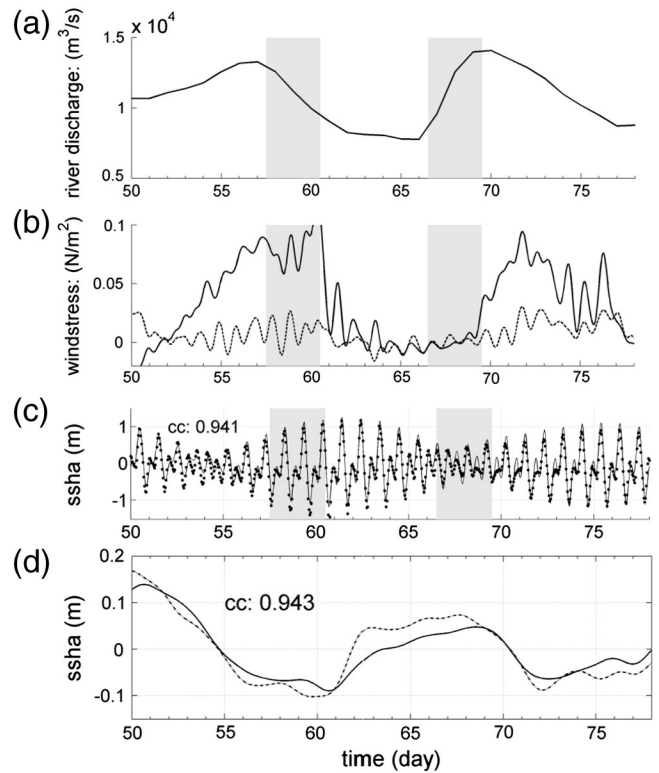
Fig. 2. Time-dependent buoyancy, wind and tide forcing illustrated by (a) river discharge (m^3 s^{-1}), (b) 12-h smoothed wind stress (Nm^{-2}) observed at Station D (solid line: along-shore component; dash line: cross-shore component), (c) tidal elevation anomaly (m) at Station A (dots), superimposed with the model simulation (solid line), (d) inertial-period (~36 h) smoothed sea surface elevation anomaly (m) at Station A (dash-dotted line: observation), superimposed with the model simulation (solid line). The gray bands indicate Periods I and II selected for energetic analysis. The numbers in (c) and (d) are the correlation coefficients. The x-axis is the number of days from the 1st June, 2000.

2.2. Model validation

The simulated sea surface elevations compare well with the observations at Stations A–H (marked in Fig. 1). Time series of the hourly sea surface elevation anomalies (Fig. 2c) and inertial period (~36 h) low-pass filtered sea surface elevation anomalies (Fig. 2d) in Station A show that the correlation coefficients of the observation and model results are larger than 0.9; the sub-tidal variation of the sea surface elevation is negatively correlated with the along-shore wind stress, which suggests that the wind- and tide-modified intertidal and sub-tidal sea surface elevation variations could be well reproduced by the model. The correlation coefficients of the sea surface elevation at other stations are all larger than 0.8, which show similar patterns as that in Station A; thus figures are not shown here for these stations. Instead, comparisons of the observed and simulated tidal harmonic constants of the two major tidal components (M$_2$ and K$_1$) at all these stations are listed in Table 1. Differences between their amplitudes and phase lags are calculated as distances following Foreman et al. (1993)

$$d = \sqrt{(H_O \cos g_O - H_S \cos g_S)^2 + (H_O \sin g_O - H_S \sin g_S)^2},$$

where (H_O, g_O) and (H_S, g_S) are the observed and modeled amplitudes and phase lags, respectively. The root mean square (RMS) error of the amplitude is

$$\sqrt{\frac{1}{2N} \sum_{i=1}^{N} |H_{Si} - H_{Oi}|^2},$$

Table 1
Comparison of the tidal harmonic constants between observation and simulation at tide gauge stations.

Station	M2					K1				
	Amplitude (cm)		Phase (deg.)		d	Amplitude (cm)		Phase (deg.)		d
	Obs.	Model	Obs.	Model		Obs.	Model	Obs.	Model	
A	43.8	42.1	306.2	303.9	2.4	41.7	42.2	331.6	338.4	5.0
B	48.1	43.1	286.2	295.2	8.7	25.2	33.1	318.6	334.7	11.3
C	58.2	55.1	326.1	335.7	10.0	42.1	49.6	334.5	337.0	7.8
D	43.4	43.1	270.3	271.5	1.0	42.5	41.8	311.0	313.8	2.2
E	36.4	35.1	268.3	272.8	3.1	42.3	43.4	313.2	311.6	1.6
F	35.5	34.2	263.8	262.2	1.6	24.0	27.9	312.1	310.9	3.9
G	33.3	32.1	254.6	253.4	1.4	23.6	25.1	309.0	308.2	1.5
H	30.1	28.7	281.4	275.8	3.2	36.4	38.2	322.7	326.7	3.2
RMS error	1.67					2.97				

where H_{Si} and H_{Oi} are the simulated and observed amplitudes at Station i, and N is the total number of observation stations. Generally, the tidal harmonic constants obtained from the model compare well with those from the observation; the RMS errors of the amplitude are only 1.67 and 2.97 for M_2 and K_1, respectively. The tidal waves are better reproduced over the shelf, as the d is smaller than those inside the estuary, possibly because of more complicated tidal features and topography inside the PRE. Nevertheless, the tidal accuracy of the simulation is sufficient to evaluate the role of tide on plume structure.

Simulated salinity along the cross-shelf sections is compared with that observed during the first upwelling period between days 53 and 60 (Fig. 3). Observations show that the low salinity plume occupies the top 10 m about 50 km off-shore, and the high-salinity bottom water moves upward onshore. The model outputs are interpolated to the time and location of the observation stations, and then plotted.

The model could reasonably capture the basic structure of the plume, but there are still discrepancies between the simulated and the observed plume. The discrepancies are not notably improved when we use different spin-up time, thus they are likely due to some simplifications utilized in the model implementation (e.g. spatially uniform wind forcing and initial condition, approximation of a constant ratio of the river discharge along the outlets of eight distributaries, and not considering the surface heat flux, etc.).

Nevertheless, the model with simplification could reasonably capture the general structure and basic response of the plume (as shown by the simulated surface salinity and observed SeaWiFS Chl-a concentration in Fig. 5 in Zu and Gan (2014)). Hence, we have modest confidence in the model performance in reproducing the responses of the plume to wind and tide forcing, and will use the simulated results for further discussion and analysis.
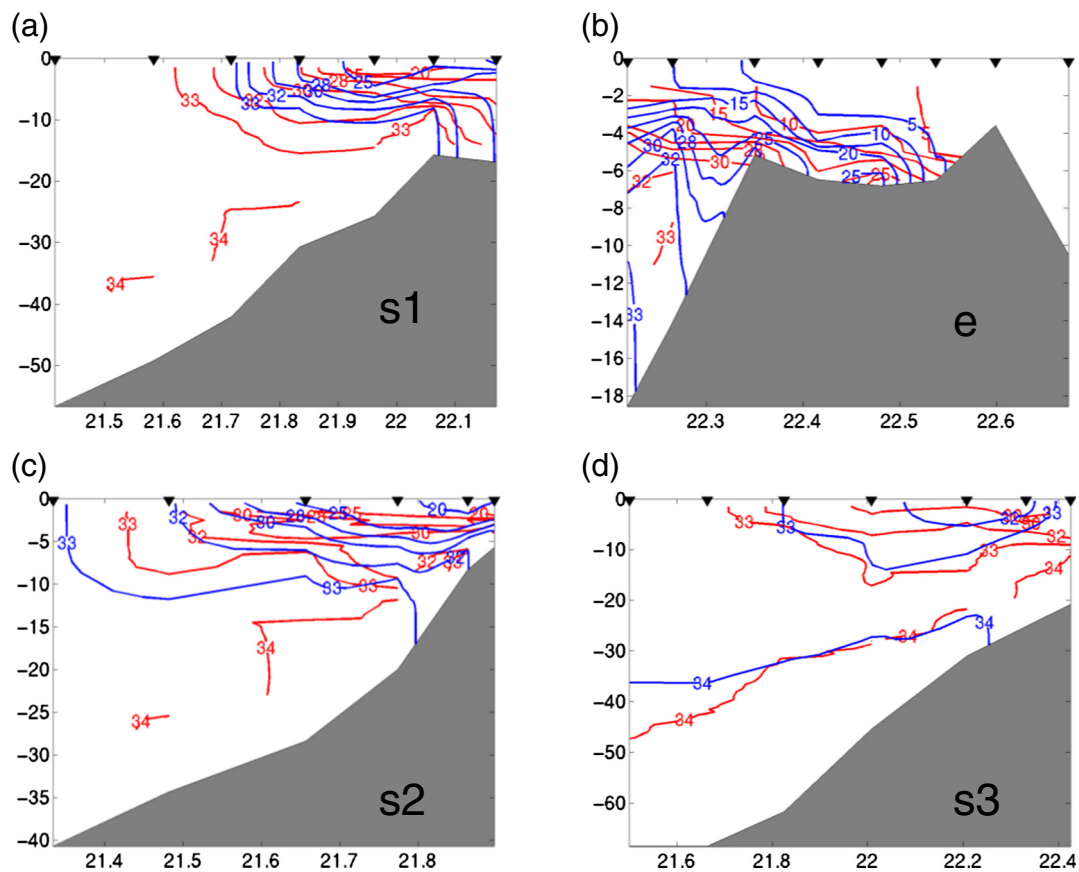
Fig. 3. Comparison of observed (red) and simulated (blue) salinity along the cross-shelf sections (locations marked by red dots in Fig. 1) during the first upwelling period. (a) Section s1 over the middle shelf, (b) Section e along the axial of the PRE, (c) Section s2 over the western shelf, and (d) Section s3 over the eastern shelf. The locations of the observation stations are shown by the inverted triangles. (For interpretation of the references to colour in this figure legend, the reader is referred to the web version of this article.)

2.3. Numerical experiments

To differentiate the roles of wind and tide forcing on the time-dependent features of the plume and stratification, two additional numerical experiments are carried out. They are the same as the standard case except for excluding either wind or tide forcing. The three cases discussed in this paper are named WRT, WR, and RT, respectively, in which "W" stands for wind, "R" stands for river, and "T" stands for tide.

3. Plume structure in response to wind and tide forcing

3.1. Horizontal shape of the plume

The horizontal shape of the plume is roughly denoted by the daily-averaged 32-psu isohaline, similar as that used in the Columbia River plume by Hickey et al. (1998), as it fits the edge of the fresh water plume well around the PRE region (Fig. 3 in this paper and Fig. 5 in Zu and Gan (2014).). And this is also because the time-dependent salinity variation of ambient shelf water is very small compared to that of the plume water. The model results averaged on days 52, 56, 60, and 67 are used to study the sub-tidal evolution of the plume under different forcing (Table 2). The shapes of the plume at the surface in WRT and WR cases (Fig. 4a, c) show greater variability compared to their shapes at bottom (Fig. 4b, d), as wind impacts the plume and current at the surface directly.

During neap tide on day 52 when the wind is weak enough to be disregarded, the plume spreads westward against the coast in all cases with no bulge formed (red lines in Fig. 4), and shows typical subcritical feature. On day 56, when the upwelling favorable wind and tidal amplitude start to grow stronger with the increase of river discharge, the plume at the sea surface (black lines in Fig. 4) is much larger in size and is advected southeastward by the surface Ekman current except for RT case. The shape and extension of the plume in WRT case resemble those of WR case, but differ from RT case, which suggests the more important role of wind forcing on the plume over the shelf in a sub-tidal frame.

When the strongest upwelling favorable wind coincides with spring tide and reduced river discharge on day 60, the wind- and tide-induced mixing is the strongest, and the plume (green lines in Fig. 4) shrinks to a narrow eastward spreading tongue. However, the plume tongue in the case without tide (WR case) spreads about 90 km further eastward than the standard case (WRT case). This indicates that strong tide could significantly affect the plume shape over the shelf. However, this does not mean that the shorter plume tongue in WRT case is directly caused by increased tidal mixing over the shelf. The difference is probably due to the modified plume properties (buoyancy and thickness) in the near-shore region (as reflected in the different shape of the plume at the bottom around the entrance of the estuary, and more low-salinity water is trapped in this region when the tidal mixing is included), which affects the plume shape in the offshore region (Fong and Geyer, 2001; Lentz, 2004).

On day 67, when the upwelling favorable wind relaxes to become a weak downwelling favorable wind, the tidal amplitude decreases and the river discharge rate is similar to that on day 60, the plume (blue lines in Fig. 4) starts to spread westward against the coast again. Meanwhile, the plume over the eastern shelf continues its eastward spreading to form an elongated low-salinity tongue, and it shows bidirectional

spreading pattern. This is because of different responses of the coastal current to the upwelling wind relaxation over the western shelf (reverses to flow westward) and the eastern shelf (keeps flowing eastward) (Zu and Gan, 2014). Another thing to note is, when comparing the blue (day 67) and green (day 60) lines, we found that the surface plume area on day 67 is larger than that on day 60, although the river discharge rate on days 61–66 is smaller than that on days 54–59. Obviously, the increasing tendency of the surface plume range due to the weakened tide and wind mixing far exceeds the shrinking tendency caused by reduced river discharge. Weaker mixing with stronger stratification keeps low-salinity water above the halocline and less low-salinity water being trapped inside the estuary; thus, a larger horizontal plume area appears at the surface over the shelf.

The edge of the plume at the bottom approximately follows the 5–10 m isobaths, and its shape is not as variable as that at the surface; the edge of the westward narrow plume against the coast almost remains at the same location in the RT case. In the WR case (without tide), the variation of the edge of the plume at the bottom and the intrusion of higher salinity tongues along the two channels in the lower half of the PRE are more distinct than and differ from the other two cases, which indicates that tide is more important than wind in determining the location of the plume front at bottom in the estuary.

It is not hard to conclude that wind is dominant for the shape of the plume at the sea surface over the deeper offshore region, while tide is dominant for the shape of the plume at bottom in the shallower near-shore region. However, the change of the structure of the plume in the near-shore region also modifies its shape off-shore. Variation of wind- and tide-induced mixing from upwelling to upwelling relaxation period and from spring to neap tide period has a stronger influence on the horizontal distribution of the plume over the shelf than the normal change of river discharge rate.

### 3.2. Vertical structure of the plume

The vertical structures of the plume and salinity diffusivity ($sdiff = \frac{\partial}{\partial z}(K_V \frac{\partial s}{\partial z})$, in which K_V is vertical eddy diffusivity, s is salinity and z is the vertical coordinate, here we consider only the vertical component as the horizontal component is several magnitudes smaller) along the axial section of the PRE (marked in Fig. 1) are shown in Fig. 5. The positive and negative values of $sdiff$ indicate increasing and decreasing tendency of salinity, respectively. The large positive and negative values of $sdiff$ appear vertically in pairs at places with strong vertical mixing and reflect the region with high mixing rate.

A large magnitude of $sdiff$ appears in the middle and lower PRE when tidal mixing is stronger (Fig. 5b, c, i, k), and it shows distinct sping–neap variation inside the estuary for WRT and RT cases. Accordingly, the structures of the plume inside the PRE are similar for WRT and RT cases, and the plume front at the bottom advances and retreats during the fortnight cycle. Besides, a large magnitude of $sdiff$ also appears at the upper layer over the shelf outside the entrance of the PRE, when the upwelling wind becomes stronger (Fig. 5b, c, f, g), which suggests a higher mixing rate and associated larger variability of plume there. The magnitude of $sdiff$ is very small in the upper estuary, since it is well-mixed and the mixing rate is low. Over the shelf farther offshore, its magnitude is much smaller than that outside the entrance of the estuary during the upwelling period, since the variability of the plume over the shelf farther offshore is mainly associated with the wind-

Table 2
Summary of the strength of buoyancy, wind and tide forcing on days 52, 56, 60, and 67. "UFW" represents upwelling favorable wind and "DFW" represents downwelling favorable wind.

Day from 1st June	River discharge (m³/s)	Wind stress (N/m²)	Tide amplitude ratio (%)	Representative forcing
52	11,080	~0.001	~34	Very weak/no wind, weak tide
56	13,176	~0.07	~45	Moderate/strong UFW, moderate tide
60	9952	~0.09	~97	Strong UFW, spring tide
67	9602	~−0.003	~30	Weak DFW, neap tide
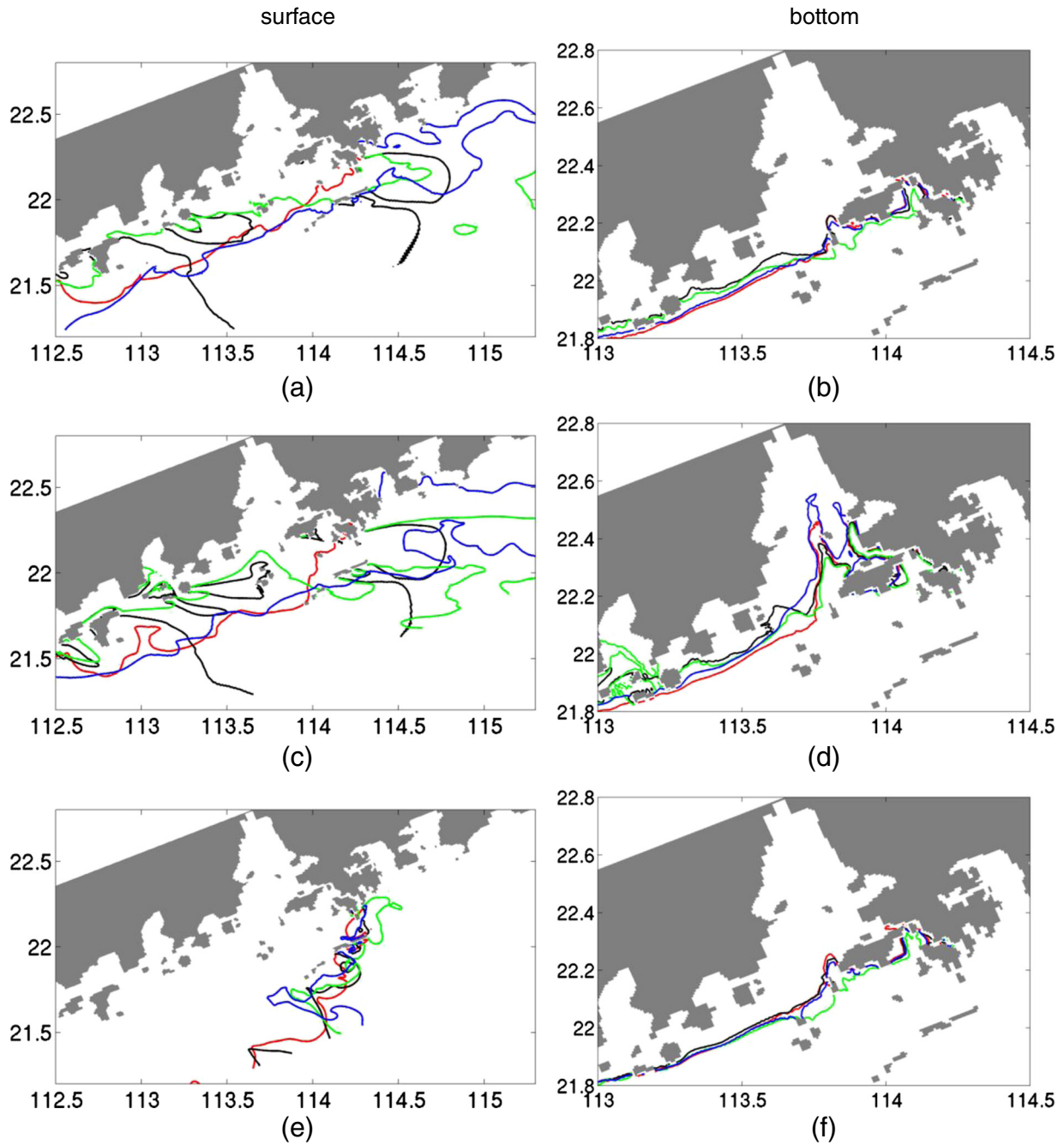
surface   bottom

Fig. 4. Surface (left) and bottom (right) salinity of 32 psu of WRT (top), WR (middle), and RT (bottom) cases averaged on day 52 (red), day 56 (black), day 60 (green), and day 67 (blue). (For interpretation of the references to color in this figure legend, the reader is referred to the web version of this article.)

driven shelf circulation induced advection processes (figures not shown here) rather than the mixing process.

Tide-induced mixing greatly weakens the stratification inside the PRE, and its influence on the plume is limited from upper estuary to the near shore region outside the PRE. The enhanced thickness of the plume by tidal mixing results in the reduced *sdiff* over the near shore region (Fig. 5c, g) (i.e. the plume is less sensitive to the wind mixing during spring tide), however the combination of wind and tide effects lead to a more complex variability of the plume than that forced by only wind or tide.

The evolution of plume structure in different cases shown in Figs. 4 and 5 clearly demonstrate that the structure of the plume in the middle and lower parts of the PRE cannot be effectively simulated without tide forcing; tidal mixing is not negligible even if we only want to study the

shelf process in this region, for the off-shore stratification and plume structure are influenced by its near-shore characteristics. The structure of the plume in the estuary is determined by the combination of the buoyancy forcing associated with river discharge and tidal mixing, and it varies with the spring–neap cycle in the middle and lower parts of the estuary. On the other hand, the vertical structure of the plume over the shelf is sensitive to the wind-induced mixing near the entrance of the estuary, but is highly influenced by wind-driven shelf circulation farther offshore.

3.3. Freshwater thickness

Freshwater thickness relative to the background salinity, s_0, is defined as the vertical integral of salinity anomaly $(s_0 - s) / s_0$. The
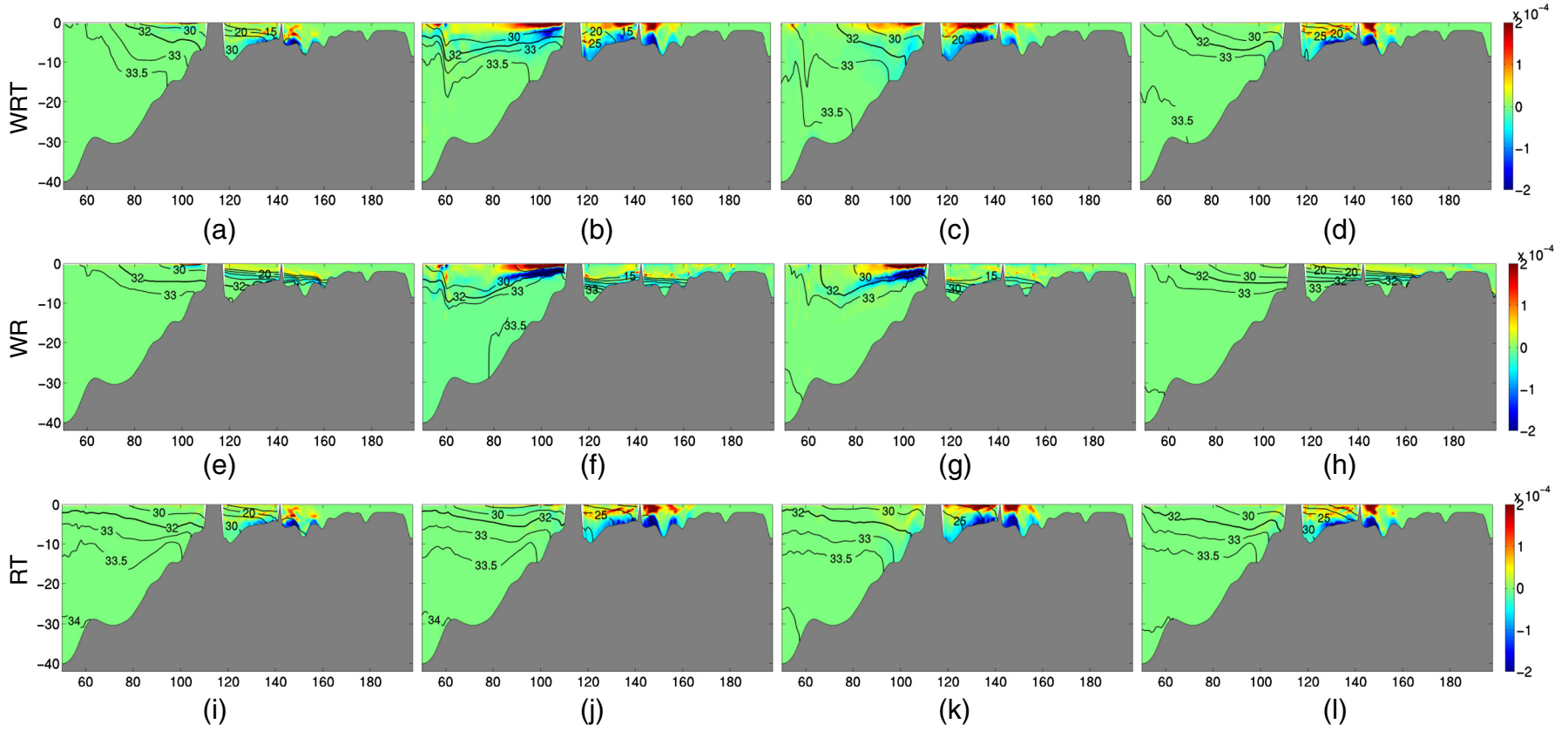
Fig. 5. Salinity (black contours) and vertical salinity diffusivity (shadings) along the axial section of the PRE for WRT (top), WR (middle), and RT (bottom) cases averaged on day 52 (first column), day 56 (second), day 60 (third), and day 67 (fourth). The numbers along the *x*-axis are the grid numbers from model's southern boundary to the northern boundary, and those along the *y*-axis are the water depth.

freshwater thickness over the shelf is highly correlated with the direction and strength of the wind; it becomes thinner (thicker) due to upwelling (downwelling), as it is stretched and advected offshore (pushed and accumulated against the coast) (Chao, 1988b; Hetland, 2005). Here, we examine the freshwater thickness of the Pearl River plume in response to tide and wind by comparing the results of WRT, WR and RT cases averaged during two periods (shown by the gray bands in Fig. 2): one is forced by strong upwelling favorable wind and spring tide (i.e., strong mixing period), and the other one is forced by very weak wind and neap tide (i.e., weak mixing period). The river discharge averages during these two periods have similar values, about 1.1×10^4 m^3 s^{-1} and 1.2×10^4 m^3 s^{-1}, respectively.

The thickness of the freshwater in the PRE mainly follows the isobaths, with the thickest part appears along the two narrow deep channels (Fig. 6a). There is not much variation of the freshwater thickness in the upper PRE, as the water is well-mixed and the mixing rate is low, and the plume is not sensitive to the change of wind- and tide-mixing. In the middle and lower parts of the PRE, the thickness of the

freshwater shows significant variation between Period I and Period II, especially for the WR case. This suggests again that the more stratified plume is more sensitive to the change of the mixing and is prone to higher mixing rate.

The range and thickness of the freshwater over the shelf show more notable variation, as advection becomes stronger. During Period I, the range and thickness of the freshwater in the WRT over the shelf is the smallest (Fig. 6a), as more low-salinity water is trapped inside the estuary due to tidal mixing and the freshwater over the shelf is quickly advected away by the wind-driven circulation and is mixed with the high salinity shelf water. During Period II (Fig. 6b), when vertical mixing is significantly reduced and the wind-driven offshore transport is relaxed, the freshwater over the shelf becomes thicker.

Unlike those in the narrower estuaries that receive lower river discharge, the structure and response of the freshwater plume and related salinity diffusivity show distinct characteristics in different parts of the PRE and adjacent shelf system, which could be divided into upper, middle, lower estuary and shelf regions. And the contributions from wind-
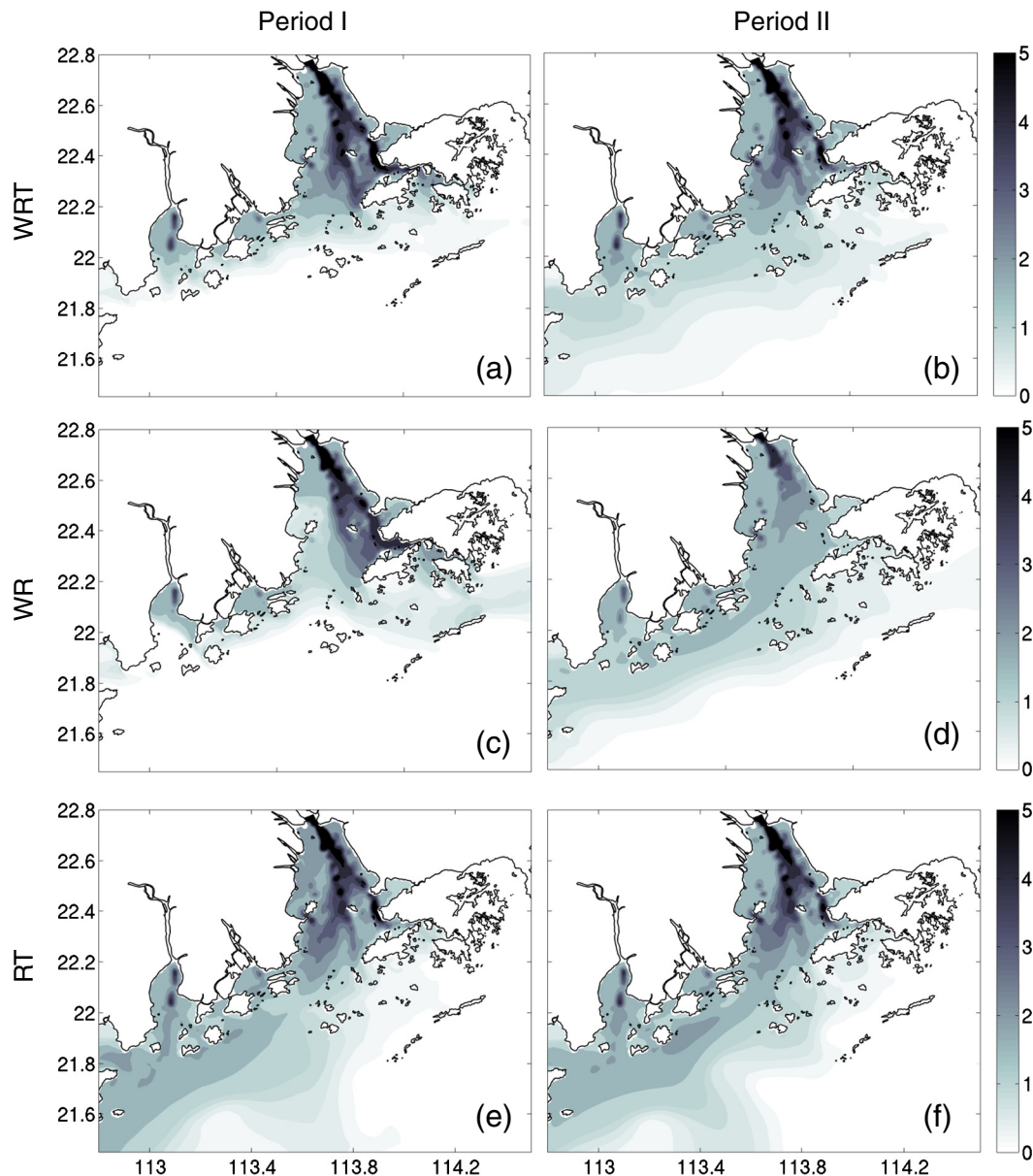
Fig. 6. Freshwater thickness of WRT (top), WR (middle), and RT (bottom) cases averaged during Period I (left) with strong upwelling favorable wind and spring tide, and Period II (right) with weak wind and neap tide.

and tide-induced mixing on plume structures in different regions are quantitatively evaluated through mechanical energy analysis in the next section.

4. Relative contribution of wind- and tide-induced mixing

Mechanical energy is required to advect and mix fresh water with saline water, and to change the stratification and thickness of the buoyant plume. In this section, we evaluate the relative importance of wind- and tide-induced mixing in different regions by comparing the mechanical energy terms in the three cases. Similar as MacCready et al. (2009), we extend their study by evaluating the energy terms in different simulations and by dividing the estuary into three regions to examine the function of the PRE in transforming fresh water into saline water. Unlike the Columbia River Estuary, the PRE has a bell shape and a wide entrance connecting to the open ocean. The river plume shows characteristics of buoyant coastal front inside the PRE (Dong et al., 2004).

Following Weisberg and Zheng (2003), Zhong and Li (2006), and MacCready et al. (2009), the mechanical energy budget could be written as (see Appendix A for detailed derivation):

$$dTE = -advTE - PW + WW - Dbot - Dint + BUOY + R. \qquad (4.1)$$

In which, dTE is local change of the total mechanical energy; $advTE$ is the flux of mechanical energy into the control volume by horizontal advection; PW is the divergence of pressure work; WW is the work done by sea surface wind stress; $Dbot$ is the energy dissipation due to bottom stress; $Dint$ is the energy dissipation by vertical shears of the horizontal velocity that is integrated in the interior portion of the selected region (i.e., vertically from the first model velocity grid point above the bottom); $BUOY$ is the buoyancy flux via vertical diffusion; R is the residual term that includes calculation error, energy dissipation from horizontal

shear of horizontal velocity and the energy contribution from horizontal diffusive fluxes of TE, which are relatively small.

We average Eq. (4.1) over Periods I and II as defined in Section 3. Period I is during a strong upwelling favorable wind with spring tide, representing a period of strong mixing. Period II is during an upwelling relaxation period with very weak wind and neap tide, representing a period of weak mixing. Each time interval includes six M_2 tidal cycles. The local change rate of the energy, dTE, is smaller than the other terms. In order to compare the roles of wind- and tide-induced mixing on the structure of the plume, we mainly focus on the forcing terms (PW and WW), dissipation terms ($Dbot$ and $Dint$) and buoyancy terms ($BUOY$) as MacCready et al. (2009) did. The horizontal distributions of the vertically-integrated terms during these two periods are shown in Figs. 7–11.

The divergence of pressure work, PW, of WRT case is positive inside the PRE and two smaller estuaries (Huang Mao Hai and Mo Dao Men), which are located on the west side of the PRE, during both periods (Fig. 7a, b). The maximum PW during these two periods appears at the entrance of Huang Mao Hai and Mo Dao Men, and in the middle of the PRE. The PW of the RT case has a structure similar to that of the WRT case, with a little difference (the value is almost zero) over the shelf (figures not shown here). For the WR case (Fig. 7c, d), PW shows a totally different pattern from the cases with the tidal forcing: PW is negative along the west sides of the estuaries when upwelling favorable wind is strong, but it is more than an order of magnitude smaller than that in the WRT and RT cases. This difference suggests that the tide-induced PW plays a dominant role in the estuary regions, and the estuarine circulation gains kinetic energy from tide-induced PW but loses energy to wind-induced PW. The volume-integrated PW (Table 3) shows that it is a major forcing term (more than 10 times larger than the WW term) for the WRT case, except during Period I over the shelf where WW is larger than PW. This implies that WW becomes more important over the shelf. The value of PW decreases from Period I to Period
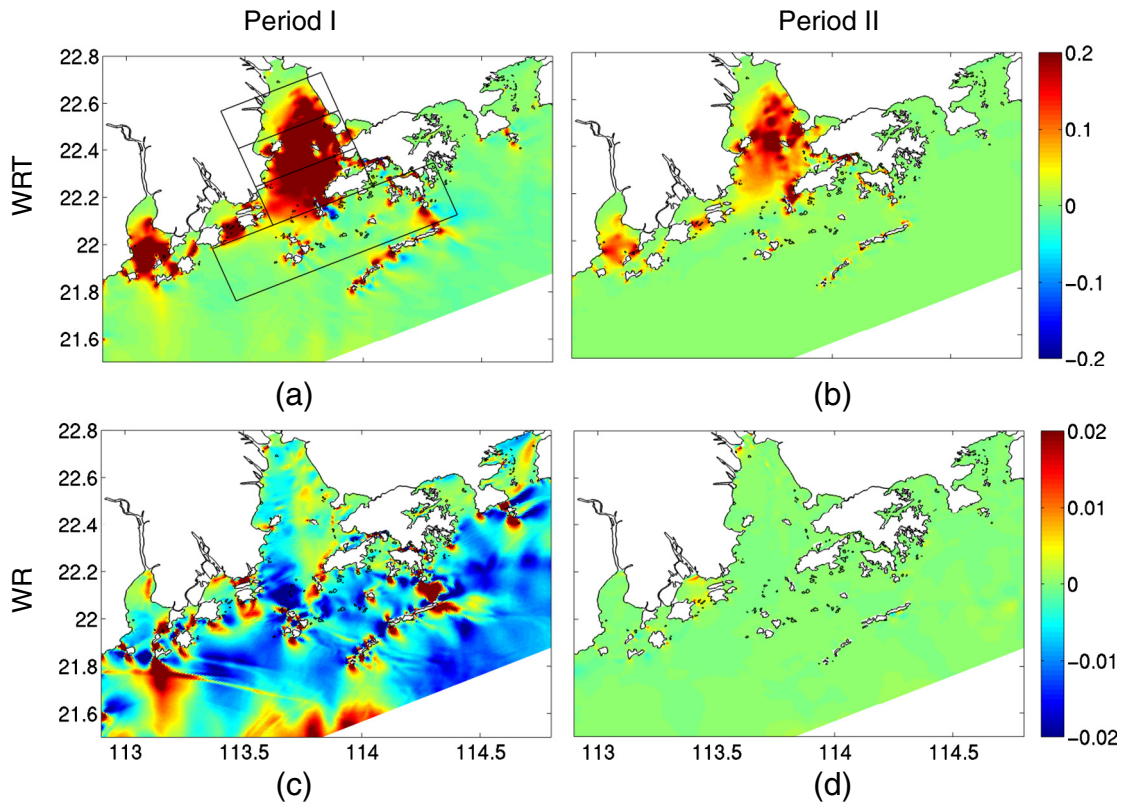

Fig. 7. Vertically-integrated pressure work term (Wm^{-2}) of WRT (upper) and WR (lower) cases during Period I (left) and Period II (right). The black boxes in (a) mark the regions of "upper," "middle," and "lower" estuary and the shelf for volume integration.
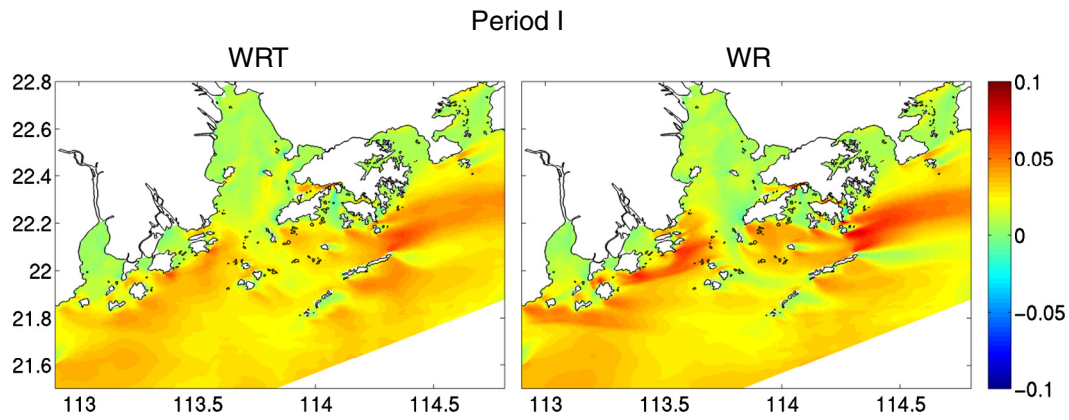
Period I

Fig. 8. Vertically-integrated wind stress work term (Wm^{-2}) of WRT (left) and WR (right) cases during Period I.

II. The amount of reduction is larger in the lower PRE and the shelf region (about 70%) than in the upper and middle PRE (about 50%) in the WRT and RT cases. The well-mixed plume in the upper estuary and the salt wedge structure at the entrance indicate that tide-induced PW input mainly acts to mix the plume and enhance the potential energy (Fig. 5).

Wind stress does positive work in both estuary and shelf (Fig. 8) during period I, but it is close to zero during period II (Figures are not shown here). The WW terms in the WR and WRT cases are similar, with a large value appears along the shallow coastal region and the plume region. It is relatively larger in the WR case than in the WRT case in both estuary and shelf regions (Table 3). This is probably because tide tends to decelerate the response of current to the wind by enhanced vertical mixing

and reduced efficiency of the WW term in the upper water column, thus inhibits the advection of the plume by wind-driven current. WW is the major forcing term in the WR case, as it is about 5 times (10 times) larger than PW in the PRE region (shelf region). WW acts to advect and mix the plume by increasing both kinetic and potential energy.

Energy dissipation due to bottom friction, $Dbot$, is negative. In the WRT case, its distribution looks like that of PW, with the largest magnitude in the middle of the PRE (Fig. 9a, b). Like the PW term, $Dbot$ in the RT case also shows a similar pattern and magnitude inside the estuary as the WRT case, and differs a little from the WRT case over the shelf (figures not shown). However, the magnitude of $Dbot$ inside the estuary in the WR case is more than two orders of magnitude smaller than that forced by tide, as tide is predominant for the bottom energy dissipation
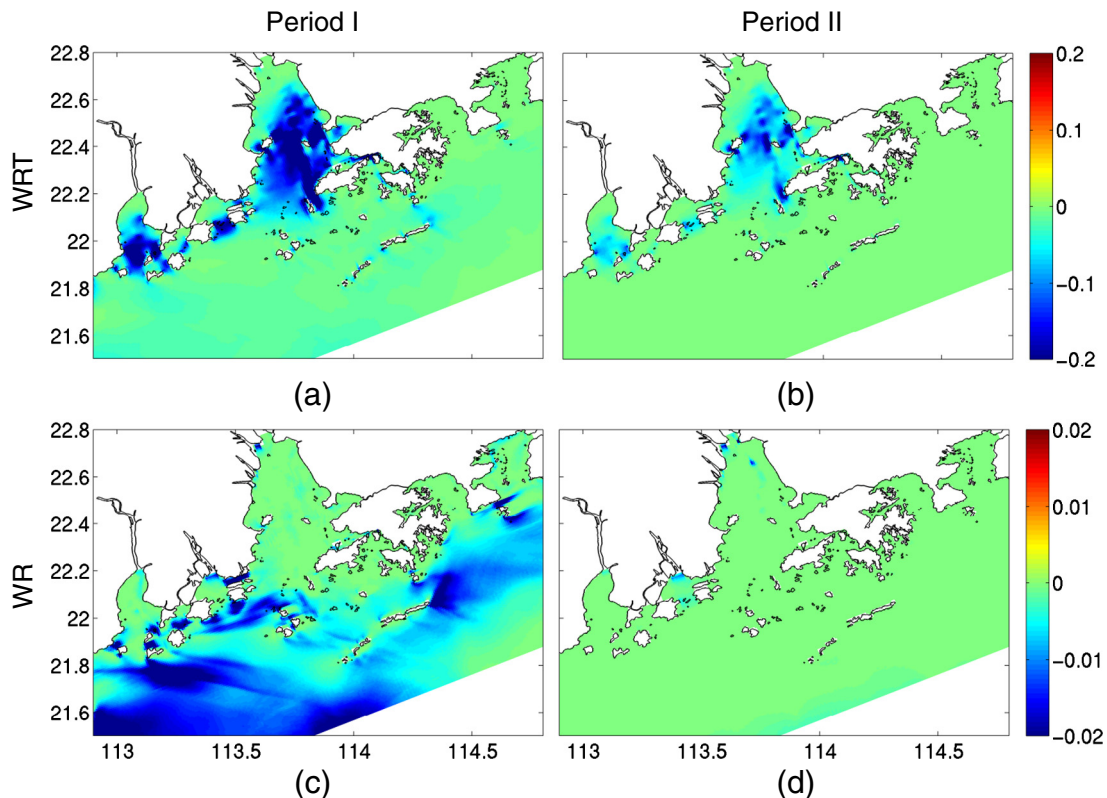

Fig. 9. Similar to Fig. 7, except for energy dissipation due to bottom friction, D_{bot}.
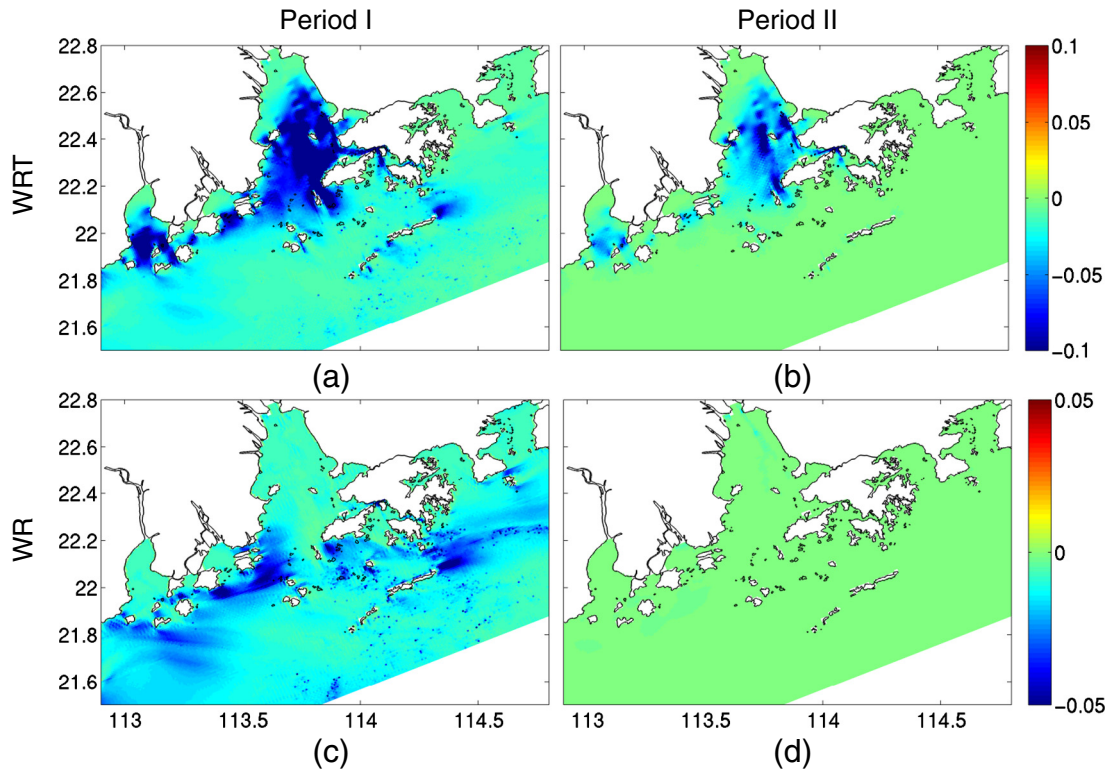
Fig. 10. Similar to Fig. 7, except for dissipation by vertical shears of horizontal velocity in the interior region, D_{int}.

in the estuary region. The distribution of interior dissipation by vertical shear of horizontal velocity, $Dint$, has a pattern similar to $Dbot$ (Fig. 10). Its magnitude is larger than $Dbot$ in the WR case, but is about 30–50% smaller than $Dbot$ in the WRT and RT cases during Period I, except for the shelf region in the WRT case, where it is notably increased and becomes larger than $Dbot$ when the wind forcing is considered (Table. 3).
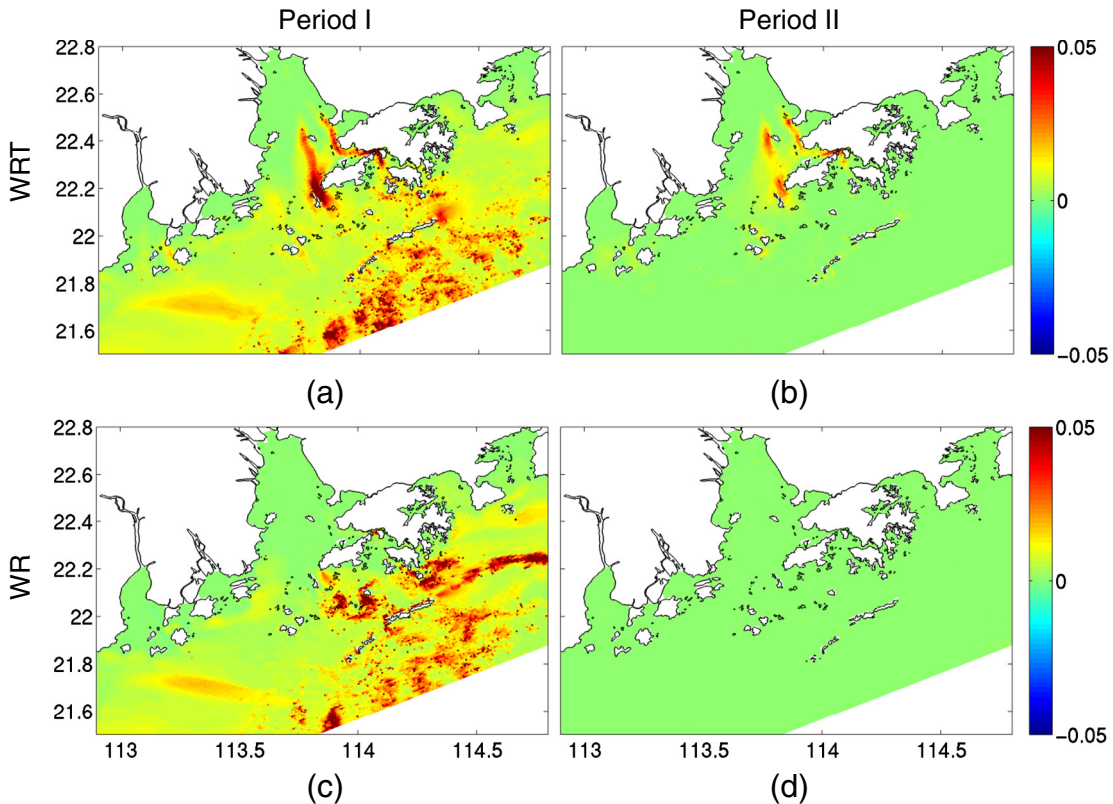

Fig. 11. Similar to Fig. 7, except for buoyancy flux, $BUOY$.

Table 3
Temporally-averaged and volume-integrated major mechanical energy terms in four different regions around the Pearl River Estuary (indicated in Fig. 7a) in WRT, WR and RT cases. "U," "M," "L," and "S" stand for the upper, middle, and lower estuary, and the shelf, respectively. The names for these five energy terms are defined in the text.

(Energy term units: 10^6 W)		Period I				Period II			
		U (1.7 km³)	M (2.9 km³)	L (5.1 km³)	S (51 km³)	U	M	L	S
WRT	PW	55.8	225	191	57.6	31	100.8	54.9	17.7
	WW	4.0	7.5	13	76.6	0.1	0.3	0.7	1.5
	D_{bot}	−34.1	−130.2	−100.2	−56.4	−19.9	−57.8	−29.5	−10.2
	D_{int}	−18.8	−75.5	−73.1	−75.3	−9.2	−36.1	−24.5	−9.3
	BUOY	0.3	3.5	8.4	22.4	0.2	3.2	4.9	3.9
WR	PW	−0.8	−1	−3.6	−6.6	0.1	0.03	−0.02	0.6
	WW	5.1	7.6	14.6	84.3	0.2	0.4	0.5	1.6
	D_{bot}	−0.3	−0.6	−0.9	−16.5	−0.2	−0.08	−0.04	−0.5
	D_{int}	−3.8	−5.7	−10.1	−48.9	−0.4	−0.6	−0.5	−1.8
	BUOY	0.2	0.4	1.7	29	0.2	0.4	0.5	1.3
RT	PW	57.8	232.8	197.8	50.3	31.4	102.1	55.6	16
	WW	0	0	0	0	0	0	0	0
	D_{bot}	−34.6	−131.6	−103.7	−34.1	−20.1	−58.1	−29.7	−9.4
	D_{int}	−16.9	−74.1	−65.8	−27.1	−9.4	−36.6	−24.9	−8.2
	BUOY	0.4	4.2	6.6	6.2	0.2	3.4	5	3

The strongest and positive buoyancy flux, *BUOY*, appears along the two channels in the middle and lower estuary in both WRT (Fig. 11a, b) and RT cases (figures are not shown), while large *BUOY* also appears in the plume region over the shelf in both WRT and WR cases (Fig. 11). The *BUOY* term in the WRT and RT cases is larger than that in the WR case inside the PRE, but smaller in the shelf region during period I (Table 3). It is greatly reduced during Period II, especially in the lower PRE and over the shelf.

The mixing efficiency (*BUOY*/|*Dbot* + *Dint*|) (Figs. 12 and 13) increases from the upper PRE (about 1–5%) to the shelf region (about 10–40%) during period I, and interestingly it is enhanced during Period II when the physical forcing and related vertical mixing decrease. The mixing efficiency in the WR case is apparently larger than that in the WRT and RT cases. This implies that the plume in the upper and middle PRE could be mixed rather well with tide forcing, the structure of the plume is not sensible to the change of vertical mixing, while the plume along the deep channels in the lower PRE and over the shelf is more susceptible to the strength of wind- and tide-induced mixing. Therefore, similar to the distribution of the mixing efficiency, the sensibility of the structure of the plume to the change of wind- and tide-induced mixing gradually increase from the upper to the lower estuary and

shelf, and from shallower coastal region to the deeper channels and off shore regions.

5. Discussion

The salt balance has been used to study the adjustment of estuarine circulation and stratification to the changes of river flow and tidal mixing by MacCready, (1999). His result shows that both stratified and well-mixed estuaries respond more rapidly to the change of forcing than the intermediate stratified ones, while intermediate estuaries are more sensitive to the change. Responses of the plume to the variation of wind and tide in different regions of the system could be further studied through the salt balance, as indicated by the mixing efficiency that the sensitivity of the plume to the mixing could vary significantly in space and time under different forcing.

The salinity equation is written as:

$$\underbrace{\frac{\partial s}{\partial t}}_{srate} + \underbrace{\mathbf{u} \cdot \nabla s}_{sadv} = \underbrace{\frac{\partial}{\partial z}\left(K \frac{\partial s}{\partial z} \right)}_{sdiff}, \qquad (5.1)$$

in which *s* is salinity, u is velocity vectors (u, v, w), *K* is eddy diffusivity. It is clear from Fig. 14 that upper PRE is well-mixed and variation of the plume is dominated by the advection process, the plume is not sensitive to the change of vertical mixing. The *sadv* term becomes larger from upper PRE to the shelf, and *sdiff* shows spring–neap variation in the deep channel of the lower PRE. However, advective-diffusive balance becomes dominant in the deep channel in the middle and lower PRE, thus the plume is not sensitive to the change of vertical mixing either. The domain averaged *sadv* is still dominant in the middle and lower PRE, because the estuary is shallow and well-mixed despite the two narrow deep channels. The variation of the plume is related to the estuarine circulation that is controlled by both the gravitational circulation and shelf upwelling intrusion (Zu and Gan, 2014). There are dramatic changes over the shelf, *sdiff* shows the variation with the strength of upwelling favorable wind, and the plume is jointly controlled by the advection and diffusion processes.

6. Summary

A three-dimensional circulation model that resolves both the estuary and part of the shelf was used to simulate the sub-tidal responses of the plume to wind and tide forcing in the PRE and its
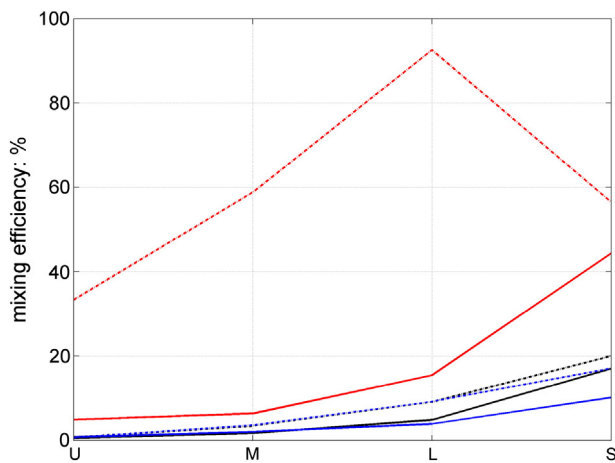
Fig. 12. The mixing efficiency (*BUOY*/|D_{bot} + D_{int}|) of WRT (black), WR (red), and RT (blue) averaged in the "upper", "middle", "lower" and "shelf" region during Period I (solid line) and Period II (dashed line). (For interpretation of the references to color in this figure legend, the reader is referred to the web version of this article.)
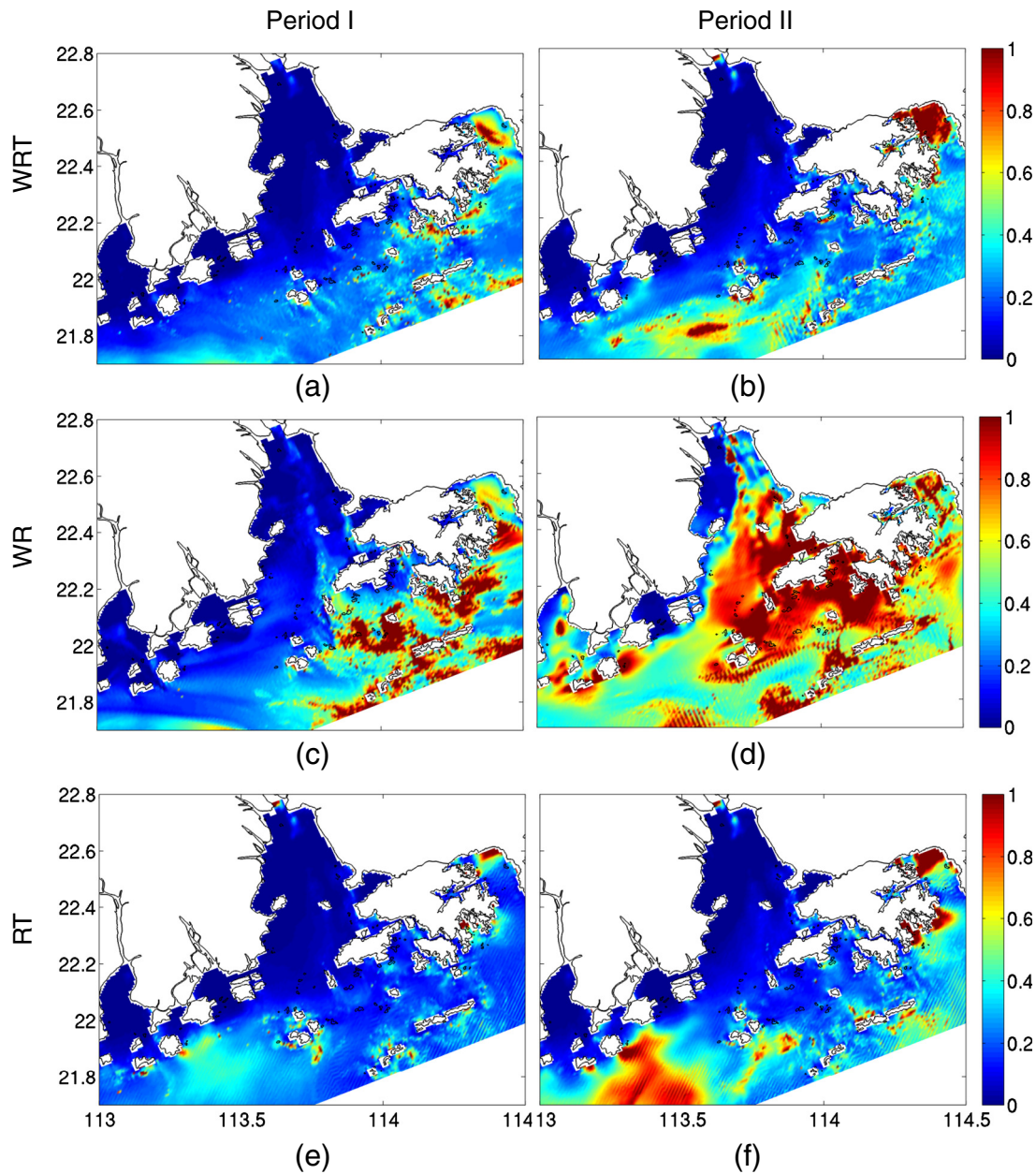
Fig. 13. Vertically-integrated mixing efficiency of WRT (upper) and WR (lower) cases during Period I (left) and Period II (right).

adjacent shelf. The model shows moderate ability to reproduce the tide- and wind-induced sea surface elevation variation and the structure of the plume, when compared with the observation from the tide gauges and cruises. Mechanical energy analysis was carried out to evaluate the relative contributions from wind and tide to the mixing and structure of the plume. We expanded MacCready et al.'s (2009) study by including two more numerical experiments that are forced without either tide or wind, and dividing the PRE into "upper", "middle" and "lower" parts, as the PRE is a bell-shaped and wide estuary.

Model results show the freshwater plume and associated mixing efficiency respond differently to the wind and tide forcing in different dynamical regions in the PRE. Specifically, wind is the dominant forcing of the plume over the shelf region, since it helps to spread and mix the plume through wind-driven coastal current. Tide plays a more important role in the estuary and shallower near-shore

region, and mainly affects the vertical structure of the plume through enhanced mixing. The change of the near-shore plume structure by tide also influences its off-shore shape. Tidal mixing tends to trap more low-salinity water inside the estuary, while up-welling favorable wind tends to spread the low-salinity water sea-ward. The sensitivity of the plume to the change of the wind and tide forcing and related vertical mixing vary significantly in different times and regions in this system, as it is well-mixed in the shallower estuarine region, but stratified in the deeper channels and shelf. The two physical forcings act to increase the kinetic energy of the system through surface stress work and divergence of the pressure work. The appearance of maximum forcing and dissipation in the middle PRE and at the entrances of other smaller estuaries suggests that tidal mixing makes the middle PRE act like an estuarine entrance, where the transition of the river plume into a coastal buoyant current occurs.
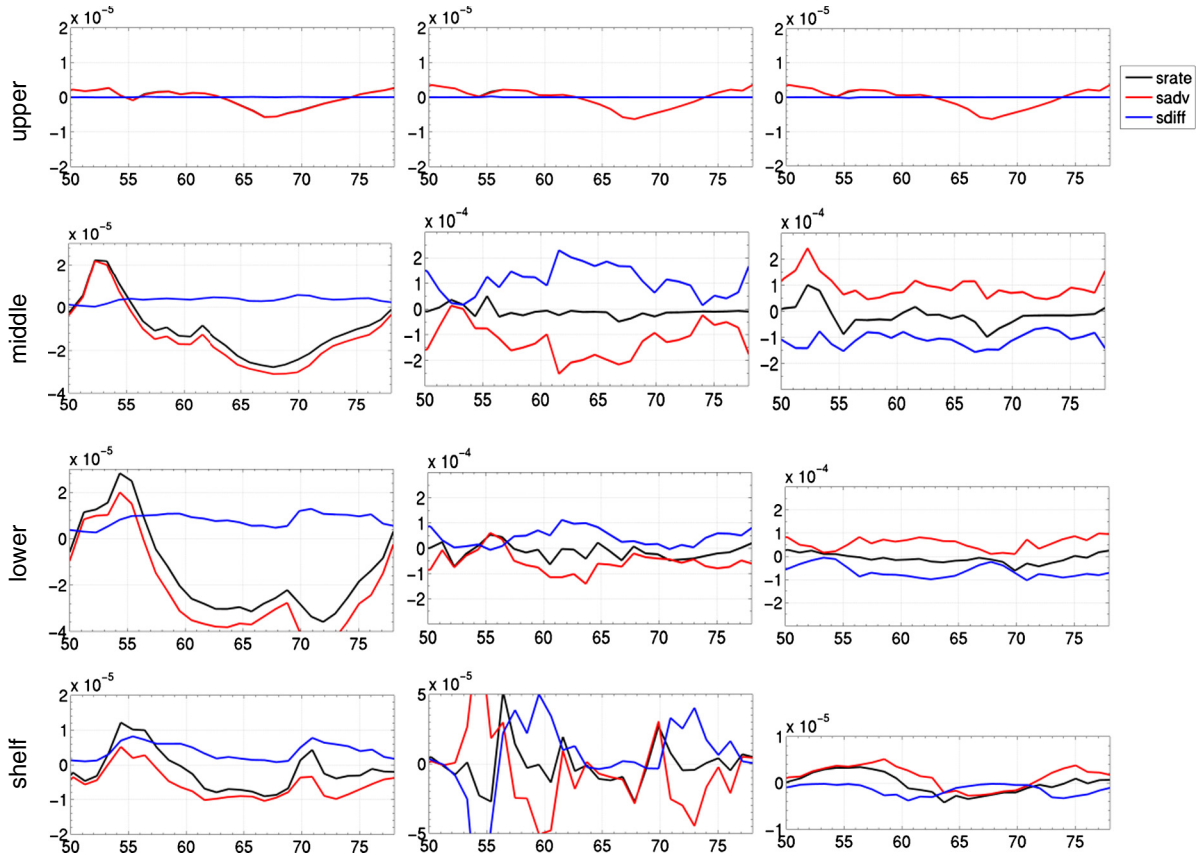
Fig. 14. Time series of the salt balance terms of WRT case in upper, middle, lower PRE and the shelf region. The values on the left column are averaged in the domains shown in Fig. 1. The middle and right columns show the value at points along the deep channel in the surface and bottom layers respectively. The x-axis is the number of days from 1st June, 2000.

This study also indicates that tidal mixing should not be disregarded even if we are interested only in the shelf process around this region, for the plume's size and structure over the shelf are highly correlated with its near-shore structure that is determined by tide.

Appendix A. Mechanical energy equations

Following Weisberg and Zheng (2003), Zhong and Li (2006), and MacCready et al. (2009), we derive the energy equations from the momentum, incompressibility, and density equations:

$$\frac{D\vec{U}}{Dt} = -f \times \vec{U} - \frac{1}{\rho_0}\nabla P + \nabla \cdot \left(K_M\nabla\vec{U}\right), \tag{A1}$$

$$\nabla \cdot \vec{U} = 0, \tag{A2}$$

$$\frac{D\rho}{Dt} = \nabla \cdot (K_M\nabla\rho), \tag{A3}$$

where $\vec{U}$ is the horizontal velocity vector (u, v). As the vertical velocity w makes little contribution to the kinetic energy, it is not included in the kinetic energy calculation here. $D(\,)/Dt = \partial(\,)/\partial t + \vec{U}\cdot\nabla$ is the material derivative, f is the Coriolis parameter, P is pressure, ρ_0 is constant background density (1025 kg m^{-3}), and ρ is the full density. K_M is eddy viscosity (including both vertical and horizontal components). The equation of kinetic energy per unit volume, $KE = (1/2)\rho_0\vec{u}^2$ is obtained by taking $\rho_0\vec{U}\cdot$ (Eq. (A1)):

$$\frac{DKE}{Dt} = -\nabla \cdot \left(P\vec{U}\right) + \nabla \cdot \left(\rho_0 K_M\vec{U}\cdot\nabla\vec{U}\right) - \rho_0 K_M(\nabla\vec{u})^2. \tag{A4}$$

The equation of potential energy per unit volume, $PE = \rho gz$, is obtained by taking gz (Eq. (A3)):

$$\frac{DPE}{Dt} = \rho gw + \nabla \cdot (gzK_D\nabla\rho) - gK_D\frac{\partial\rho}{\partial z}. \tag{A5}$$

Thus, the volume integral of the total mechanical energy ($TE = KE + PE$) could be obtained by combining the volume integrals of

Eqs. (A4) and (A5):

$$\underbrace{\frac{\partial}{\partial t}\int_V TEdV}_{(1)} = \underbrace{-\int_S \vec{U} TEdS}_{(2)} - \underbrace{\int_V \nabla\cdot(P\vec{U})dV}_{(3)} + \underbrace{\int_A \rho_0(u_s\tau_s^x + v_s\tau_s^y)dA}_{(4)} - \underbrace{\int_A \rho_0(u_b\tau_b^x + v_b\tau_b^y)dA}_{(5)}$$

$$-\underbrace{\int_V \rho_0 K_{MV}\left[\left(\frac{\partial u}{\partial z}\right)^2 + \left(\frac{\partial v}{\partial z}\right)^2\right]dV}_{(6)} + \underbrace{\int_V \left(\rho g w - g K_{MV}\frac{\partial \rho}{\partial z}\right)dV}_{(7)}$$

$$-\underbrace{\int_V \rho_0 A_M\left[\left(\frac{\partial u}{\partial x}\right)^2 + \left(\frac{\partial v}{\partial x}\right)^2 + \left(\frac{\partial u}{\partial y}\right)^2 + \left(\frac{\partial v}{\partial y}\right)^2\right]dV}_{(8)} + \underbrace{\int_S A_M \nabla TEdS}_{(9)}$$

(A6)

where V is the volume of a chosen geographical region, S is the area of the lateral sides of the selected region, A is the surface or bottom areas of this region, τ is stress, subscripts s and b denote surface and bottom, respectively, and K_{MV} and A_M are the vertical and horizontal eddy viscosity coefficients, respectively.

The nine terms in (A6) are defined as follows.

(1) is local change of the total mechanical energy, dTE;
(2) is the flux of mechanical energy into the control volume by horizontal advection, $advTE$;
(3) is the divergence of pressure work, PW;
(4) is the work done by sea surface wind stress, WW;
(5) is the energy dissipation due to bottom stress, $Dbot$;
(6) is the energy dissipation by vertical shears of the horizontal velocity that is integrated in the interior portion of the selected region (i.e., vertically from the first model velocity grid point above the bottom), $Dint$;
(7) is the buoyancy flux via vertical advection and diffusion, $BUOY$;
(8) is similar to (6), but is due to the horizontal shear of horizontal velocity; and
(9) is the horizontal diffusive fluxes of TE into the selected column.

The buoyancy flux by vertical advection, $\rho g w$, converts between the kinetic and potential energy. When the full vertical momentum equation is used, $\rho g w$ would be canceled from $BUOY$ term. Thus, in the discussion of the buoyancy flux, only the part caused by vertical diffusion is considered. The energy contribution from terms (8) and (9) is relatively small, if we combine them with the calculation errors into the residual term, R, Eq. (A6) could be rewritten as:

$$dTE = -advTE - PW + WW - Dbot - Dint + BUOY + R. \tag{A7}$$

References

Chao, S.-Y., 1988a. River-forced estuarine plumes. J. Phys. Oceanogr. 18, 72–88.
Chao, S.-Y., 1988b. Wind-driven motion of estuarine plumes. J. Phys. Oceanogr. 18, 1144–1166.
Chao, S.-Y., 1990. Tidal modulation of estuarine plumes. J. Phys. Oceanogr. 20, 1115–1123.
Chao, S.-Y., Boicourt, W.C., 1986. Onset of estuarine plumes. J. Phys. Oceanogr. 16, 2137–2149.
Choi, B., Wilkin, J.L., 2007. The effect of wind on the dispersal of the Hudson River Plume. J. Phys. Oceanogr. 37, 1878–1897.
Dong, L.X., Su, J.L., Wong, L.A., Cao, Z.Y., Chen, J.C., 2004. Seasonal variation and dynamics in the Pearl River plume. Cont. Shelf Res. 24, 1761–1777.
Fennel, W., Mutzke, A., 1997. The initial evolution of a buoyant plume. J. Mar. Syst. 12, 53–68.
Fong, D.A., Geyer, W.R., 2001. Response of a river plume during an upwelling favorable wind event. J. Geophys. Res. Oceans 106 (C1), 1067–1084.
Foreman, M.G.G., Henry, R.F., Walters, R.A., Ballantyne, V.A., 1993. A finite element model for tides and resonance along the north coast of British Columbia. J. Geophys. Res. Oceans 98, 2509–2531.
Gan, J., Li, L., Wang, D., Guo, X., 2009. Interaction of a river plume with coastal upwelling in the northeastern South China Sea. Cont. Shelf Res. 29, 728–740.
Garcia-Berdeal, I., Hickey, B.M., Kawase, M., 2002. Influence of wind stress and ambient flow on a high discharge river plume. J. Geophys. Res. Oceans 107 (C9), 3130.
Garvine, R.W., 2001. The impact of model configuration in studies of buoyant coastal discharge. J. Mar. Res. 59, 193–225.
Guo, X., Valle-Levinson, A., 2007. Tidal effects on estuarine circulation and outflow plume in the Chesapeake Bay. Cont. Shelf Res. 27, 20–42.
Haidvogel, D.B., Arango, H.G., Hedstrom, K., Beckmann, A., Malanotte-Rizzoli, P., Shchepetkin, A.F., 2000. Model evaluation experiments in the North Atlantic Basin: simulations in nonlinear terrain-following coordinates. Dyn. Atmos. Oceans 32, 239–281.
Harrison, P.J., Yin, K., Lee, J.H.W., Gan, J., Liu, H., 2008. Physical–biological coupling in the Pearl River Estuary. Cont. Shelf Res. 28, 1405–1415.
Hetland, R.D., 2005. Relating river plume structure to vertical mixing. J. Phys. Oceanogr. 35, 1667–1688.
Hickey, B.M., Pietrafesa, L.J., Jay, D.A., Boicourt, W.C., 1998. The Columbia River plume study. Subtidal variability in the velocity and salinity fields. J. Geophys. Res. Oceans 103, 10,339–10,368.
Hunter, E.J., Chant, R.J., Wilkin, J.L., Kohut, J., 2010. High-frequency forcing and subtidal response of the Hudson River plume. J. Geophys. Res. Oceans 115, C07012.
Ji, X., Sheng, J., Tang, L., Liu, D., Yang, X., 2011a. Process study of circulation in the Pearl River Estuary and adjacent coastal waters in the wet season using a triply-nested circulation model. Ocean Model. 38, 138–160.
Ji, X., Sheng, J., Tang, L., Liu, D., Yang, X., 2011b. Process study of dry-season circulation in the Pearl River Estuary and adjacent coastal waters using a triple-nested coastal circulation model. Atmos. Ocean 49 (2), 138–162.
Kourafalou, V.H., Oey, L.-Y., Wang, J.D., Lee, T.N., 1996a. The fate of river discharge on the continental shelf. Part I: modeling the river plume and the inner shelf coastal current. J. Geophys. Res. Oceans 101 (C2), 3415–3434.
Kourafalou, V.H., Lee, T.N., Oey, L.-Y., Wang, J.D., 1996b. The fate of river discharge on the continental shelf. Part II: transport of low-salinity waters under realistic wind and tidal forcing. J. Geophys. Res. Oceans 101 (C2), 3435–3455.
Lentz, S., 2004. The response of buoyant coastal plumes to upwelling-favorable winds. J. Phys. Oceanogr. 34, 2458–2469.
Li, M., Zhong, L., Boicourt, W.C., 2005. Simulations of Chesapeake Bay estuary: sensitivity to turbulence mixing parameterizations and comparison with observations. J. Geophys. Res. Oceans 110, C12004.
Liu, Y., MacCready, P., Hickey, B.M., Dever, E.P., Kosro, P.M., Banas, N.S., 2009. Evaluation of a coastal ocean circulation model for the Columbia River plume in summer 2004. J. Geophys. Res. Oceans 114, C00B04.
Luo, L., Zhou, W., Wang, D., 2012. Responses of the river plume to the external forcing in Pearl River Estuary. Aquat. Ecosyst. Health Manag. 15 (1), 62–69.
MacCready, P., 1999. Estuarine adjustment to changes in river flow and tidal mixing. J. Phys. Oceanogr. 29, 708–726.
MacCready, P., Banas, N.S., Hickey, B.M., Dever, E.P., Liu, Y., 2009. A model study of tide- and wind-induced mixing in the Columbia River estuary and plume. Cont. Shelf Res. 29, 278–291.
Mellor, G.L., Yamada, T., 1982. Development of a turbulence closure model for geophysical fluid problems. Rev. Geophys. Space Phys. 20, 851–875.
Otero, P., Ruiz-Villarreal, M., Peliz, A., 2008. Variability of river plumes off Northwest Iberia in response to wind events. J. Mar. Syst. 72, 238–255.
Ou, S., Zhang, H., Wang, D., 2007. Horizontal characteristics of buoyant plume off the Pearl River Estuary during summer. J. Coast. Res. SI 50, 652–657.
Ou, S., Zhang, H., Wang, D., 2009. Dynamics of the buoyant plume off the Pearl River Estuary in summer. Environ. Fluid Mech. 9, 471–492.
Rong, Z., Li, M., 2012. Tidal effects on the bulge region of Changjiang River plume. Estuar. Coast. Shelf Sci. 97, 149–160.
Shchepetkin, A.F., McWilliams, J.C., 2005. The Regional Ocean Modeling System: a split-explicit, free-surface, topography following coordinates ocean model. Ocean Model. 9, 347–404.
Simpson, J.H., 1997. Physical processes in the ROFI regime. J. Mar. Syst. 12, 3–15.
Simpson, J.H., Brown, J., Matthews, J., Allen, G., 1990. Tidal straining, density currents, and stirring in the control of estuarine stratification. Estuaries 26, 1579–1590.
Song, Y., Haidvogel, D.B., 1994. A semi-implicit ocean circulation model using a generalized topography-following coordinate system. J. Comput. Phys. 115 (1), 228–244.
Warner, J.C., Geyer, W.R., Lerczak, J.A., 2005. Numerical modeling of an estuary: a comprehensive skill assessment. J. Geophys. Res. Oceans 110, C05001.
Weisberg, R.H., Zheng, L., 2003. How estuaries work: a Charlotte Harbor example. J. Mar. Res. 61, 635–657.
Whitney, M.M., Garvine, R.W., 2005. Wind influence on a coastal buoyant outflow. J. Geophys. Res. Oceans 110, C03014.
Wolanski, E., Spagnol, S., King, B., Ayukai, T., 1999. Patchiness in the Fly River plume in Torres Strait. J. Mar. Syst. 18, 369–381.
Wong, L.A., Chen, J.C., Xue, H., Dong, L.X., Su, J.L., Heinke, G., 2003a. A model study of the circulation for the Pearl River Estuary (PRE) and its adjacent coastal waters: 1. Simulations and comparison with observations. J. Geophys. Res. Oceans 108 (C5), 3156.
Wong, L.A., Chen, J.C., Xue, H., Dong, L.X., Guan, W.B., Su, J.L., 2003b. A model study of the circulation in the Pearl River Estuary (PRE) and its adjacent coastal waters: 2. Sensitivity experiments. J. Geophys. Res. Oceans 108 (C5), 3157.
Xing, J., Davies, A.M., 1999. The effect of wind direction and mixing upon the spreading of a buoyant plume in a non-tidal regime. Cont. Shelf Res. 19, 1437–1438.
Xue, H., Chai, F., 2001. Coupled physical-biological model for the Pearl River Estuary: a phosphate limited subtropical ecosystem. The Proceedings of the Seventh International Conference on Estuarine and Coastal Modelling. ASCE, New York, pp. 913–927.
Yankovsky, A.E., Chapman, D.C., 1997. A simple theory for the fate of buoyant coastal discharges. J. Phys. Oceanogr. 27, 1386–1401.
Zhong, L., Li, M., 2006. Tidal energy fluxes and dissipation in the Chesapeake Bay. Cont. Shelf Res. 26, 752–770.
Zu, T., Gan, J., 2009. Process-oriented study of the circulation and river plume in the Pearl River Estuary: response to the wind and tidal forcing. Adv. Geosci. 12, 213–230 (b672-v12-ch16, Ocean Science Series).
Zu, T., Gan, J., 2014. A numerical study of coupled estuary-shelf circulation around the Pearl River Estuary during summer: responses to variable winds, tides and river discharge. Deep-Sea Res. II. http://dx.doi.org/10.1016/j.dsr2.2013.12.010.
Zu, T., Gan, J., Erofeeva, S.Y., 2008. Numerical study of the tide and tidal dynamics in the South China Sea. Deep-Sea Res. I 55, 137–154.